Using topological insulator proximity to generate perfectly conducting channels in materials without topological protection

2014 New J. Phys. 16 113058

(http://iopscience.iop.org/1367-2630/16/11/113058)

New Journal of Physics
The open access journal at the forefront of physics
Deutsche Physikalische Gesellschaft DPG | IOP Institute of Physics

Using topological insulator proximity to generate perfectly conducting channels in materials without topological protection

Sven Essert, Viktor Krueckl and Klaus Richter
Institut für Theoretische Physik, Universität Regensburg, D-93040 Regensburg, Germany
E-mail: Sven.Essert@ur.de

Received 7 August 2014, revised 26 September 2014
Accepted for publication 7 October 2014
Published 24 November 2014
New Journal of Physics **16** (2014) 113058
doi:10.1088/1367-2630/16/11/113058

Abstract
We show that hybrid structures of topological insulators (TI) and materials without topological protection can be employed to create perfectly conducting channels (PCCs) hosted in the non-topological part. These states inherit the topological protection from the proximity of the TI but are more fragile to time-reversal symmetry breaking because of their extended character. We explore their formation in the band structure of model hybrid systems as well as realistic heterostructures involving HgTe/CdTe-based two-dimensional TIs and show how their appearance can be understood in terms of an effective boundary condition. Using numerical quantum transport calculations for the HgTe/CdTe material system we propose two experimental settings which allow for the detection of the induced PCCs, both in the localized and diffusive regime, by means of magneto conductance and shot noise.

Keywords: topological insulators, heterostructures, perfectly conducting channel, boundary conditions, transport

1. Introduction

One important feature of the topological classification of insulators [1] is the existence of gapless states at interfaces between materials which differ in their topological quantum number.

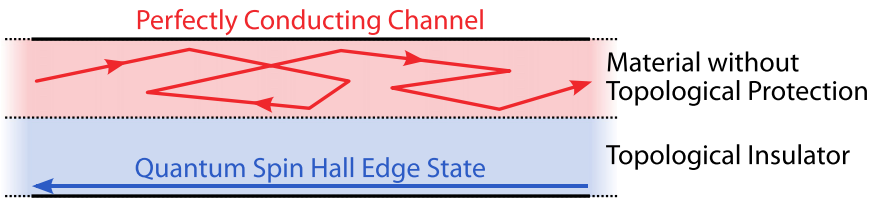

Figure 1. Sketch of a non-topological strip in proximity to a topological insulator inducing a perfectly conducting channel in the normal material.

In this way, one can understand the formation of quasi one-dimensional (1D) edge channels in quantum Hall systems and in two-dimensional (2D) topological insulators (TI) at the interface between the topologically non-trivial insulator and the trivial insulating vacuum. These edge channels carry the unique property of being perfectly conducting, even in presence of impurity scattering, corresponding to transmission eigenvalues of one. Such quantized, spin-polarized channels along the boundaries of a 2D TI crystal have already been detected experimentally [2] and give rise to peculiar conductance phenomena such as the quantum spin Hall effect [3, 4].

In this paper we show that perfectly conducting channels (PCCs) can be induced in materials *without* topological protection by the proximity of a 2D TI as sketched in figure 1. In such a hybrid structure the non-topological material could be a (disordered) metal, a gated semiconductor or even a conventional Anderson insulator. Such a setup exploits the hybridization of the upper TI edge state with the bulk states of the normal material, leading to an imbalance of left and right moving states in the normal material and thereby to a PCC therein. The emergence of PCCs in isolated non-topological systems has been earlier predicted for carbon nanotubes [5] and graphene nanoribbons [6, 7]. There the PCC was shown [6] to arise from an uneven separation of left and right moving states associated with specific (valley) symmetries [7]. However, since atomic defects or short-ranged impurity potentials break this symmetry, PCCs are rather fragile in these graphene-based systems and have not yet been observed therein. Contrarily, the proximity-induced PCCs reported here are robust against any kind of disorder as long as time-reversal symmetry is preserved, even in presence of spin–orbit coupling.

To our knowledge this phenomenon has not been discussed before in 2D heterostructures, only layers made of 2D TIs nested in 3D systems [8–10] and pure insulator heterostructures [11] have been considered very recently.

In the following section 2, we first demonstrate the emergence of a proximity-induced PCC by means of a band structure analysis within a simplified model calculation. In section 3, we will present numerical results that show the same features in HgTe/CdTe-based ribbons. Furthermore, we will study features of the PCC in quantum transport for experimentally realizable setups. In section 4, we introduce a boundary condition, which is able to mimic the proximity of a TI and induce PCCs in non-topological materials.

2. Model calculation

The appearance of a PCC in a heterostructure of a 2D TI and a usual conductor can already be understood in terms of a simple model system which captures the important physical features. It assumes a waveguide structure which is periodic in the x-direction and laterally consists of a finite strip of a usual conductor with width W bordering a semi-infinite TI plane at one side. Throughout this work we model the electronic structure of a 2D HgTe/CdTe quantum-well by

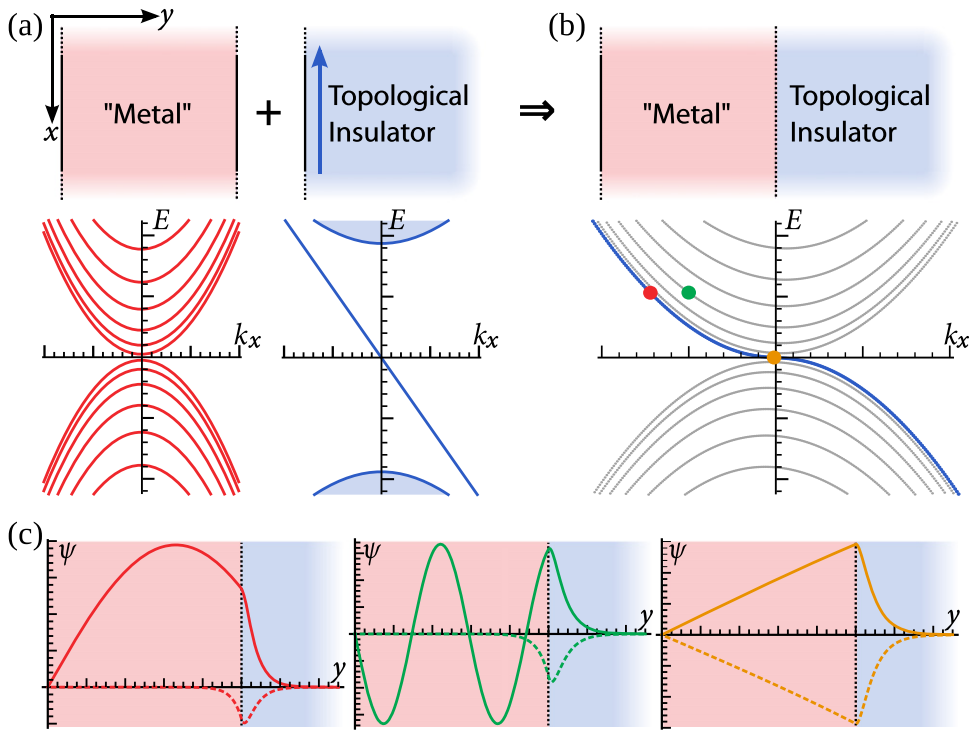

Figure 2. Minimal model illustrating the emergence of a perfectly conducting channel. Band structure of (a) a non-topological strip (left) and a semi-infinite topological insulator plane (right), (b) the combined system. 'Metal' stands for a model of a conductor with many open modes and a parabolic dispersion. (c) Wave functions for parameters marked by dots in (b). Solid/dashed lines show the first/second component of the wave functions. (These plots were obtained using the following set of parameters: $A = 5,\ B = -100,\ M = -0.05,\ W = 1000$.)

the four-band Bernevig–Hughes–Zhang (BHZ) Hamiltonian [3]

$$H = \begin{pmatrix} h(\mathbf{k}) & \begin{matrix} 0 & -\Delta \\ \Delta & 0 \end{matrix} \\ \begin{matrix} 0 & \Delta \\ -\Delta & 0 \end{matrix} & h^*(-\mathbf{k}) \end{pmatrix}, \tag{1}$$

with spin-subblock Hamiltonians

$$h(\mathbf{k}) = \begin{pmatrix} M - (B+D)\mathbf{k}^2 & Ak_+ \\ Ak_- & -M + (B-D)\mathbf{k}^2 \end{pmatrix}, \tag{2}$$

where $k_\pm = k_x \pm \mathrm{i}k_y$ and $\mathbf{k}^2 = k_x^2 + k_y^2$. The off-diagonal coupling parameter Δ in (1) describes a Dresselhaus-type spin–orbit coupling of the two spin blocks [12]. The 'metal' part[1] is modeled by the Hamiltonian (1) with $A = D = M = \Delta = 0$, describing a free electron-hole gas.

[1] We use the term 'metal' synonymously to 'material with extended states' also referring to a gated semiconductor. For simplicity we use a topologically trivial BHZ Hamiltonian and show how the PCC is induced in general. However, such approximations are not applied in the subsequent numerical simulations, which are based on realistic HgTe/CdTe heterostructures.

Confined to a finite-width strip by hard wall boundary conditions, this leads to an electron-hole symmetric parabolic band structure, as shown in figure 2(a). For the TI half plane, we use a minimal BHZ Hamiltonian h_{TI} ($h(k)$ with $D = \Delta = 0$[2]). The band structure for one spin block shown in figure 2(a) exhibits the bulk band gap and a single edge state. A coupling between the two systems is implemented by replacing the central hard wall constraint by the continuity of the wave function $\Psi(y)$ and the flux $v_y\Psi(y)$ across the interface, i.e.

$$\begin{pmatrix} 2\mathrm{i}B\partial_y & 0 \\ 0 & -2\mathrm{i}B\partial_y \end{pmatrix}\Psi(W-\epsilon) = \begin{pmatrix} 2\mathrm{i}B\partial_y & \mathrm{i}A \\ -\mathrm{i}A & -2\mathrm{i}B\partial_y \end{pmatrix}\Psi(W+\epsilon). \tag{3}$$

This leads to the secular equation

$$\frac{4B^2 f_p\left(\lambda_2 u_1 v_2 - \lambda_1 u_2 v_1\right)}{f_m \cosh\left(f_m W\right)\sinh\left(f_p W\right)} + \frac{\left(4B^2 - A^2\right)\lambda_1\lambda_2\left(u_2 v_1 - u_1 v_2\right) - 2AB\left(\lambda_1 - \lambda_2\right)\left(u_1 u_2 - v_1 v_2\right)}{f_m f_p \cosh\left(f_m W\right)\cosh\left(f_p W\right)} \tag{4}$$

$$= \frac{4B^2 f_p f_m\left(u_1 v_2 - u_2 v_1\right)}{\sinh\left(f_m W\right)\sinh\left(f_p W\right)} + \frac{4B^2 f_m\left(\lambda_2 u_2 v_1 - \lambda_1 u_1 v_2\right)}{\sinh\left(f_m W\right)\cosh\left(f_p W\right)}, \tag{5}$$

which is solved numerically to yield the band structure. Here

$$f_p = \sqrt{k_x^2 + \frac{E}{B}}, \qquad f_m = \sqrt{k_x^2 - \frac{E}{B}}, \tag{6}$$

and $u_{1/2}$, $v_{1/2}$ are the components of the decaying free solutions $\xi_{k_x}^{1/2}(y)$ in the TI-region

$$\xi_{k_x}^{1/2}(y) = \begin{pmatrix} u_{1/2} \\ v_{1/2} \end{pmatrix} \mathrm{e}^{\lambda_{1/2} y}, \tag{7}$$

$$u_{1/2} = -\frac{E + B\left(\lambda_{1/2}^2 - k_x^2\right) + M}{A\left(\lambda_{1/2}^2 - k_x\lambda_{1/2}\right)}, \tag{8}$$

$$v_{1/2} = \frac{1}{\lambda_{1/2}}, \tag{9}$$

where $h_{\mathrm{TI}}\ \xi_{k_x}^{1/2}(y) = E\ \xi_{k_x}^{1/2}(y)$. The decay coefficients (which have a negative real part as long as $|E| < |M|$) are given by

$$\lambda_{1,2} = -\sqrt{\frac{A^2 + 2B^2 k_x^2 - 2BM \mp \sqrt{A^4 + 4B^2E^2 - 4A^2BM}}{2B^2}}. \tag{10}$$

The resulting band structure, shown in figure 2(b), resembles the one of the metallic strip, but contains an extra band (marked in blue) as a remainder of the topological edge state, which does not feature the linear momentum dependence because of band repulsion due to hybridization. The wave functions at various energies in figure 2(c) reveal that *all* states are predominantly

[2] For simplicity we assume the value of the parameter B to be the same in the two regions.

localized in the metallic region and only small exponential tails remain in the TI part. Thus, we do not find evidence for an induced non-trivial topology as reported in [11], from which one would expect a new interface state forming on the outer hard wall boundary. Instead, the former edge state fully hybridizes with the metallic bands and covers the whole extended state region! In [9] the authors also observe an extended metallic state in a 3D heterostructure, which possibly inherits the protection from localization from the 3D TI. However, it is not expected to be perfectly conducting in the same way, as one will not usually observe a quantized value for the conductance for the surface transport of a 3D TI. Our results differ from the findings of [10], where a protection from hybridization for topological edge states is reported for a 2D quantum Hall insulator on top of a 3D substrate.

The above result has important consequences. Counting the bands in figure 2(b) reveals an imbalance between left and right movers (up and down movers in figure 2), which leads to a PCC at any Fermi energy. Including the other spin block and spin–orbit interaction only slightly changes this picture. Since both spin blocks feature a PCC with opposite propagation direction in the decoupled system, the combined system has an equal but *odd* number of left and right moving channels. Due to the time-reversal symmetry of the Hamiltonian, the scattering matrix can be written in a basis where it is anti-symmetric. Together with the odd number of channels, this implies a single PCC in each direction [13]. As the wave functions of all channels are predominantly localized in the metallic region, one can say that the proximity of the TI induces a single additional channel in each direction leading to one net PCC in the metallic region. In other words, the quasi 1D edge state of the TI migrates into the metallic region and forms an extended PCC. We believe that this is generally true for materials with extended states. It should provide a valuable tool to create and observe PCCs as they inherit the topological protection of the former edge channels and are expected to be stable for any disorder and interface type, as long as the latter allows for sufficient hybridization.

3. Transport signatures in HgTe/CdTe structures

For the practical observation of a PCC the semi-infinite TI plane can be replaced by a TI-ribbon in a four-lead geometry, see figure 3(a). This geometry decouples the edge channel on the lower edge of the TI from the region with the PCC. This is necessary, as the lower edge state would add another channel to the scattering matrix, make it even dimensional and therefore lift the protection of the PCC.

It is not required to assemble the heterostructure presented in figure 3(a) from two different materials. For convenience the whole system can consist of a common HgTe/CdTe quantum well with inverted band order, where only the upper (metallic) part has a Fermi energy outside the TI bandgap, a setting that can be realized by local gating. Such a setup leads to a hybridization of the upper pair of edge states of the TI with the bulk states of the metallic part, while the lower pair is still localized at the lower edge of the TI. The corresponding band structure in figure 3(b) reveals that a single spin block contains an additional right moving state, whereas the left mover is still localized at the opposite boundary in the TI region. This is indicated by the color code, which represents states located in the part without topological protection by red lines and states in the gated part by blue lines.

Furthermore, we stress that an inverted band order is not strictly necessary to induce a PCC. The bands of a gapless metallic strip shown in figure 3(c), as well as a strip with

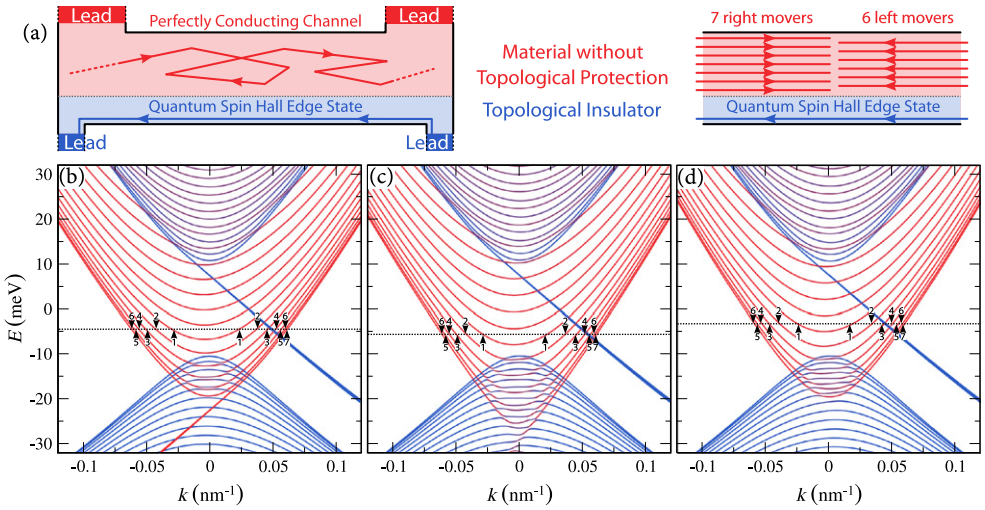

Figure 3. (a) Scheme of the four-lead geometry used for PCC observation (b)–(d) band structures for one spin block of a nanoribbon ($W = 350$ nm, HgTe/CdTe material parameters, table 1, $\Delta = 0$) with different band topology ((b) $M = -10$ meV, (c) $M = 0$ meV, (d) $M = 10$ meV) in proximity to a TI ribbon (energy offset $E_0 = 30$ meV). Colors encode the position of the corresponding wave function (localized in the metallic part: red/in the TI: blue).

conventional ordering presented in figure 3(d) also feature an additional right moving state in proximity to a TI. This implies that PCCs can be induced by the same mechanism in other semiconductors if the two materials can be coupled efficiently and the crossover of the band topology takes place in the metallic part or at the interface.

3.1. Transport in the localized regime

Experimental evidence for the induction of a PCC can be for example accomplished by means of magneto transport measurements in the localized regime. To this end, we suggest a four-terminal configuration based on a 2D-TI like HgTe/CdTe, as sketched in figure 4(a).

In the following we present numerical transport calculations based on such a HgTe/CdTe heterostructure, described by the BHZ Hamiltonian (1) using the material parameters summarized in table 1. The whole system consists of a single, spatially constant material, which is discretized on a square grid with a lattice spacing of 4 nm. We assume the material hole-doped and set the Fermi energy to $E_F = -40$ meV, such that no quantum spin Hall edge states are involved in transport and the sample behaves like a conventional metal. Furthermore, Anderson disorder is added on each lattice site. The disorder strength is set to $U_0 = 30$ meV and the length of the strip to $L = 8\,\mu$m, which leads to strong localization and a very low transmission between the right and the left side. The signatures of the strong localization are visible in the non-equilibrium local density of states (LDOS) in figure 4(b), which is calculated for a potential gradient using higher chemical potentials for the two leads at the left side. The states entering the system at the left are not able to propagate through the whole sample, which leads to a gradient in the LDOS from high densities at the left side to low densities at the right side over several orders of magnitude.

In the following, a quantum spin Hall effect is induced by gating a part of the material into the TI bandgap at the lower edge of the structure, as depicted by the blue region in figure 4(a).

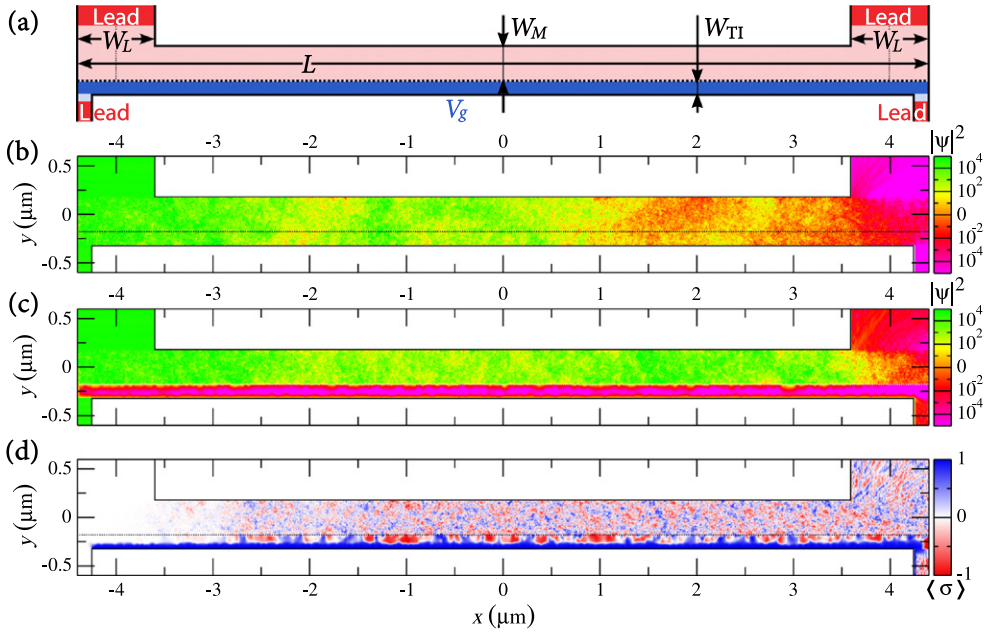

Figure 4. Setup to analyze the transport features of a perfectly conducting channel in a strongly disordered 'H-bar'. (a) Geometry of the disordered HgTe/CdTe 'H-bar' ($L = 8$ μm, $W_M = 350$ nm, $W_{TI} = 150$ nm, $W_L = 800$ nm). (b) Typical carrier distribution (local density of states) arising for a small bias with higher chemical potentials applied to the two left leads without additional gating ($E_F = -40$ meV). (c) Typical carrier distribution for a gate potential of $V_g = 40$ mV. (d) Corresponding spin polarization.

Table 1. Material parameters for HgTe/CdTe quantum wells (units in meV and nm), taken from [14].

A	B	D	M	Δ
354.5	−686	−512	−10	1.6

This expels all states from the bulk of the lower strip such that only a quantum spin Hall edge state is remaining, which shows up as the thin dark connection between the lower leads in the LDOS presented in figure 4(c). In turn a PCC is induced in the upper part of the strip, leading to a significant change in the transport characteristics between the upper two leads. As the lateral extent of the PCC in a disordered material is expected to be on the order of the localization length, the width of the strip should be smaller than this length scale to create an efficient coupling between the PCC and these upper two leads. For sufficiently wide leads a perfect coupling can be achieved, and as a result, the total transmission T_M between the upper leads will be at least one, even in presence of disorder and without localization for increasing system length. This transmission can be extracted from a set of non-local resistance measurements, as shown in the appendix. To illustrate the signatures of the PCC the transport properties of this setup are calculated for different gate potentials V_g by means of a recursive Greens function algorithm [15]. If the gated part is tuned such that the Fermi energy is in the TI bandgap, the suppressed transmission T_{TI} of the localized regime takes the quantized value $T_{TI} \approx 1$ of the quantum spin Hall edge state. This behavior of T_{TI} is shown in figure 5(a) by the solid (blue)

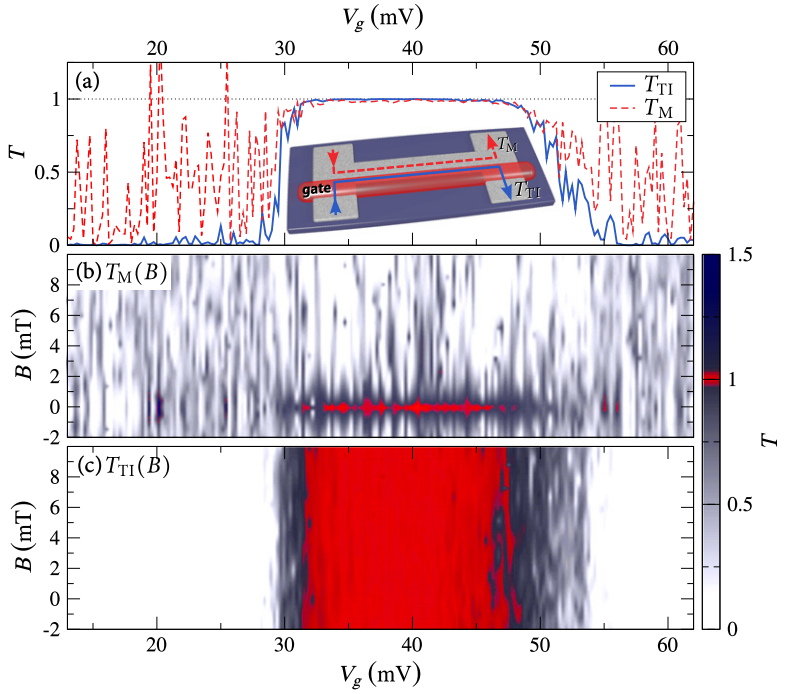

Figure 5. Quantized conductance of a perfectly conducting channel in a strongly disordered HgTe/CdTe 'H-bar' ($L = 8\,\mu$m, $W_M = 350$ nm, $W_{TI} = 150$ nm, $W_L = 800$ nm as shown in the inset). (a) Transmission T_M (red dashed) between the upper leads and T_{TI} (blue solid) between the lower leads featuring a quantized value for $V_g \in [30, 50]$ mV, where only the lower gated part is in a TI state. (b) Magnetic field dependence of transmission $T_M(B)$ (color coded) through the ungated normal part. (c) Transmission $T_{TI}(B)$ through the gated (TI) part.

line for gate voltages between 30 mV and 50 mV. Remarkably, the transmission T_M between the two upper leads exhibits the same behavior and gets quantized, although there is no material with topological protection linking the two terminals. This quantized transmission in the otherwise localized regime is a clear-cut signature of and carried by the PCC.

The different nature of the PCC compared to the quantum spin Hall edge state can be probed by a perpendicular magnetic field B. Since the PCC state is extended over the entire spatial region A of the upper strip, which can be seen in the LDOS of figure 4(c), a weak field generating a flux $A \cdot B \approx \phi_0$, where ϕ_0 is the flux quantum, is sufficient to effectively break the time-reversal symmetry. The numerical data presented in figure 5(b) shows that the conductance quantization of T_M is fully destroyed for a magnetic field of $B = 2$ mT, corresponding to ϕ_0 penetrating the device. This is not the case for the robust quantum spin Hall edge state, which is strongly localized at the lower boundary and accordingly quasi one-dimensional. As a result, the magneto transport is insensitive to magnetic fields in the mT regime, as shown for T_{TI} in figure 5(c). As a side remark, the PCC turns out to be completely spin mixed already at small spin–orbit strengths Δ, in contrast to the quantum spin Hall edge channels, which remain spin-polarized up to moderate spin–orbit strengths visible by the constant blue color in the spin density at the lower edge presented in figure 4(d). The PCC does not show this polarization, which can be seen by the patchy pattern in the upper part of the spin density.

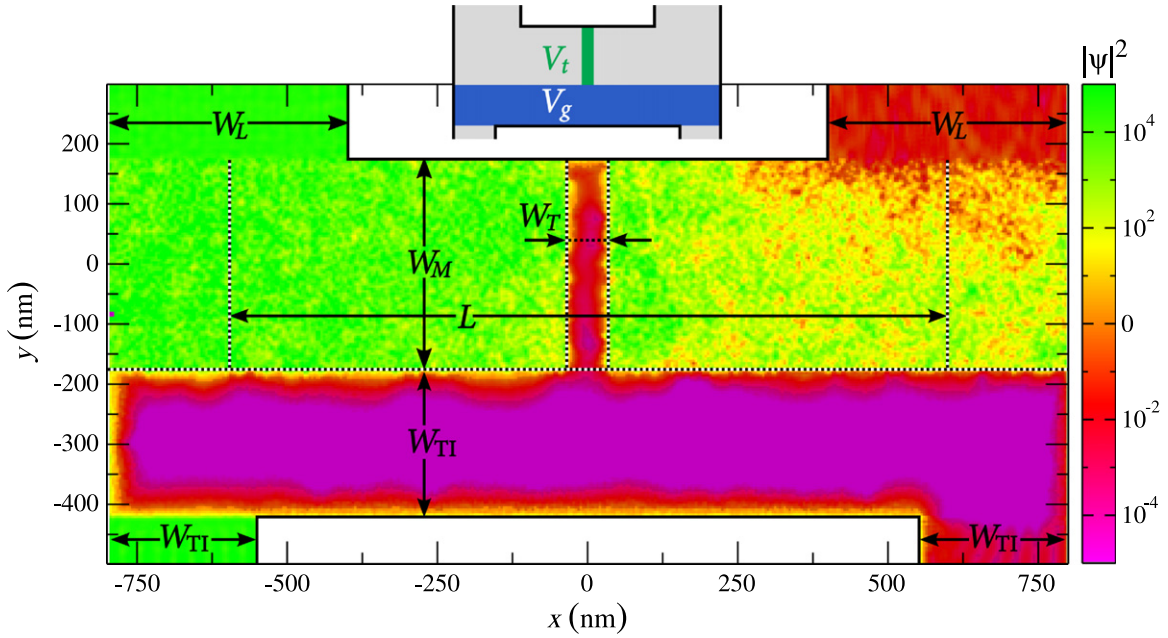

Figure 6. Tunnel setup for the detection of the perfectly conducting channel in the diffusive regime using an 'H-bar' ($L = 1.2\,\mu$m, $W_M = 350$ nm, $W_{TI} = 250$ nm, $W_L = 400$ nm, $W_T = 120$ nm) made of a HgTe/CdTe heterostructure. Typical carrier distribution arising for a small bias with higher chemical potentials applied to the left leads ($E_F = -40$ meV, dark colors represent higher densities). Lower part is tuned into the topological bandgap by $V_g = 40$ mV and the upper strip is divided into two parts by an additional tunnel barrier with $V_t = 40$ mV.

3.2. Transport through a tunnel barrier

In the previous setup a quantized conductance was used to demonstrate the emergence of a PCC in an otherwise localized region. Therefore a very long system was needed, such that all channels, except the PCC, are sufficiently localized by the impurity potential. Although the PCC is still present if L is smaller, the total transmission $T_M = \sum_n t_n$ also contains contributions $0 < t_n < 1$ of non-PCCs. In this case an additional tunnel barrier, depicted by the green bar in the sketch of figure 6, can be used to unravel the presence of the PCC. Similar to the previous setup, a gate V_g is used to induce a PCC between the upper two leads and a quantum spin Hall edge state at the lower boundary, which can be seen in the LDOS in figure 6. Furthermore, a second gate V_t is added, which acts as a tunnel barrier and separates the diffusive metal between the upper two leads in two parts, in order to reduces the contributions of the non-PCCs.

Without tunnel barrier the diffusive transport between the upper two leads results in a bimodal distribution $P(t)$ of the transmission eigenvalues t [16, 17], as shown in the upper left panel of figure 7(a). Consequently, the intermediate transmission eigenvalues mask the PCC when considering the total transmission T_M. The probability of these intermediate transmission eigenvalues can be strongly reduced by increasing the potential V_t of the tunnel barrier, as shown in figure 7(a) for $B = 0$ mT, $V_t = 40$ mV. Hence, for sufficiently high V_t the total transmission T_M is mainly carried by the PCC. As in the localized case, the protection of the PCC can be easily broken by the application of a small magnetic flux, leading to a broader distribution for the high transmission eigenvalues, shown in the right panel of figure 7(a).

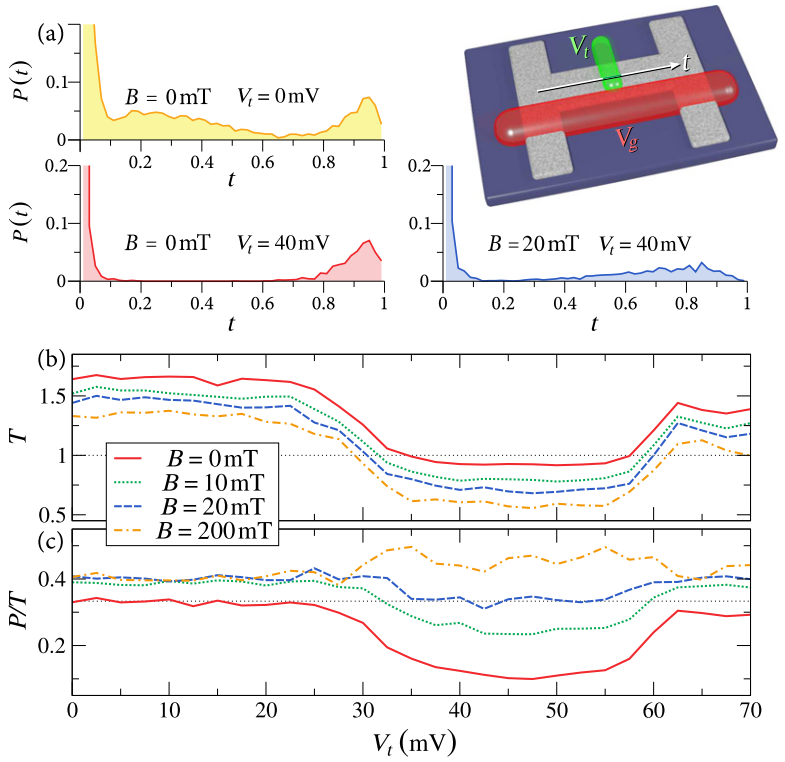

Figure 7. Tunnel setup for the detection of the perfectly conducting channel in the diffusive regime using an 'H-bar' ($L = 1\,\mu$m, $W_M = 350$ nm, $W_{\rm TI} = 150$ nm, $W_L = 400$ nm) and an additional tunnel gate V_t as shown as green bar in the inset. (a) Distribution functions of the transmission eigenvalues t (from ensemble averages over 1000 impurity configurations) for different tunnel gates V_t with and without magnetic field. (b) Average total transmission T between the upper leads with $T \approx 1$ for $B = 0$ in presence of a sufficiently strong tunnel barrier. (c) Average Fano factor P/T for the current between the upper leads featuring a strong suppression of shot noise in presence of a perfectly conducting channel.

The transition between these different probability distributions is also reflected in transport quantities, which can be experimentally probed. For example, upon raising the tunnel barrier V_t the transmission at $B = 0$ exhibits a quantized minimum, which reflects the presence of a PCC, as shown by the red line in figure 7(b) for $V_t \in [30, 60]$ mV. As expected, this feature disappears at small magnetic fields.

A more pronounced PCC signature is found in the shot noise power [18], $P = \sum_n t_n(1 - t_n)$, depending on the transmission eigenvalues t_n between the upper leads. For conventional diffusive transport the bimodal distribution leads to a universal 1/3 suppression of the shot noise ($P = T/3$, as marked by a dashed line in figure 7(c)), independent of the universality class of the material [19]. In presence of a tunnel barrier all t_n except the one of the PCC tend to zero, leading to a characteristic shot noise suppression, as shown by our numerics in figure 7(c) for $V_t \in [30, 60]$ mV. As the PCC is easily destroyed by a weak magnetic field, the shot noise suppression disappears. At finite B, in absence of the PCC the shot noise signal even increases above $P = T/3$ due to the tunnel barrier. We suggest the tunnel conductance and shot noise as promising, experimentally accessible observables to verify the TI proximity induced PCC.

4. Effective boundary condition

In the following section, we will show that the qualitative effect of the proximity of a 2D TI half-plane on a wave guide, can also be understood in terms of an effective boundary condition and that this boundary condition can be held responsible for the creation of a PCC. The derivation starts from the band structure calculation in the model system introduced in section 2. There, we found an expression for the decay constant λ of the states into the TI half plane stated in (10). In the limit, where the extent of the states inside the insulator is short compared to the width of the metallic ribbon, one can replace the TI half-plane by an effective boundary condition for the wave function $\psi(y)$ inside the metallic ribbon. In the following, we will take a limit of the material parameters which achieves this infinitely fast decay and will provide us with a suitable boundary condition. As the considered model of the TI involves many parameters, there is no unique way of doing this and hence the obtained boundary conditions will not be unique either. Even though they should be taken as exemplary, they will turn out to be conceptually simple and they will capture all important physical features.

For achieving the infinite decay constants we let $M \to -\infty$, i.e., we will consider a TI with an infinite band gap. In addition, we rescale A by choosing $A = X \cdot \sqrt{-M}$ with a parameter X having the units $\sqrt{\text{energy}} \cdot \text{length}$. If one now considers the limit $M \to -\infty$ keeping $X = \frac{A}{\sqrt{-M}} = \text{const}$, one finds for the real parts of the decay constants $\lambda_{1/2}$:

$$\lim_{M\to-\infty} \operatorname{Re}\lambda_1 = -\infty, \tag{11}$$

$$\lim_{M\to-\infty} \operatorname{Re}\lambda_2 = -\infty, \tag{12}$$

meaning that we indeed expect the wave functions not to extend into the TI. For this limit, one can derive the appropriate boundary conditions that any attached two-band Hamiltonian has to fulfill. We start from the continuity of the wave function of the metal region $\psi^M(y)$,

$$\begin{pmatrix} \psi_1^M(W) \\ \psi_2^M(W) \end{pmatrix} = c_1 \begin{pmatrix} u_1 \\ v_1 \end{pmatrix} + c_2 \begin{pmatrix} u_2 \\ v_2 \end{pmatrix}, \tag{13}$$

and the probability current $v_y \psi^M(y)$ across the boundary at $y = W$,

$$\begin{aligned}(-\mathrm{i}) v_y \begin{pmatrix} \psi_1^M(W) \\ \psi_2^M(W) \end{pmatrix} = {} & c_1 2B\lambda_1 \begin{pmatrix} u_1 \\ -v_1 \end{pmatrix} + c_2 2B\lambda_2 \begin{pmatrix} u_2 \\ -v_2 \end{pmatrix} \\ & + Ac_1 \begin{pmatrix} v_1 \\ -u_1 \end{pmatrix} + Ac_2 \begin{pmatrix} v_2 \\ -u_2 \end{pmatrix},\end{aligned} \tag{14}$$

for so far unknown constants c_1 and c_2. We are now interested in the behavior of the right-hand sides for the limit discussed above. However, as

$$\lim_{M\to-\infty} \left|u_{1/2}\right| = \lim_{M\to-\infty} \left|v_{1/2}\right| = 0, \tag{15}$$

one needs to rescale the constants to keep the wave function finite at the interface:

$$c'_{1/2} = \frac{c_{1/2}}{\sqrt{-M}}. \tag{16}$$

This way, we find

$$\psi_1^M(W) = c_1'\sqrt{-M}\,u_1 + c_2'\sqrt{-M}\,u_2, \tag{17}$$

$$\psi_2^M(W) = c_1'\sqrt{-M}\,v_1 + c_2'\sqrt{-M}\,v_2, \tag{18}$$

from (13). We can now do the limiting process on the right-hand side always keeping $X = \frac{A}{\sqrt{-M}}$ fixed, using

$$\lim_{M\to-\infty} u_1\sqrt{-M} = \underbrace{\frac{1}{2}\left(X + \sqrt{4B + X^2}\right)}_{\equiv q_1(B,\,X)}, \tag{19}$$

$$\lim_{M\to-\infty} v_1\sqrt{-M} = -\underbrace{\frac{1}{2}\left(X + \sqrt{4B + X^2}\right)}_{\equiv q_1(B,\,X)}, \tag{20}$$

$$\lim_{M\to-\infty} u_2\sqrt{-M} = \underbrace{\frac{1}{2}\left(X - \sqrt{4B + X^2}\right)}_{\equiv q_2(B,\,X)}, \tag{21}$$

$$\lim_{M\to-\infty} v_2\sqrt{-M} = -\underbrace{\frac{1}{2}\left(X - \sqrt{4B + X^2}\right)}_{\equiv q_2(B,\,X)}, \tag{22}$$

and assuming that $B < 0$ and $X > 0$. To simplify the notation we introduced the functions $q_1(B, X)$ and $q_2(B, X)$:

$$\psi_1^M(W) = c_1' q_1(B, X) + c_2' q_2(B, X), \tag{23}$$

$$\psi_2^M(W) = -c_1' q_1(B, X) - c_2' q_2(B, X). \tag{24}$$

From this, we can already find the first boundary condition

$$\psi_1^M(W) = -\psi_2^M(W). \tag{25}$$

Note that this is independent of the choice of the parameters B and X. The second boundary condition which links the currents is, however, more complicated and does depend on the choice of B and X. It can be simplified by additionally choosing $X = 2\sqrt{-B}$, which will then imply

$$q_1\left(B, X = 2\sqrt{-B}\right) = q_2\left(B, X = 2\sqrt{-B}\right) = \sqrt{-B}\,. \tag{26}$$

If we now subtract the two components of (14)

$$\begin{aligned}&\mathrm{i}\left(v_y\psi^M\right)_2(W) - \mathrm{i}\left(v_y\psi^M\right)_1(W)\\ &\quad = c_1'\left(2B\lambda_1 + A\right)(u_1 + v_1)\sqrt{-M} + c_2'\left(2B\lambda_2 + A\right)(u_2 + v_2)\sqrt{-M}\,,\end{aligned} \tag{27}$$

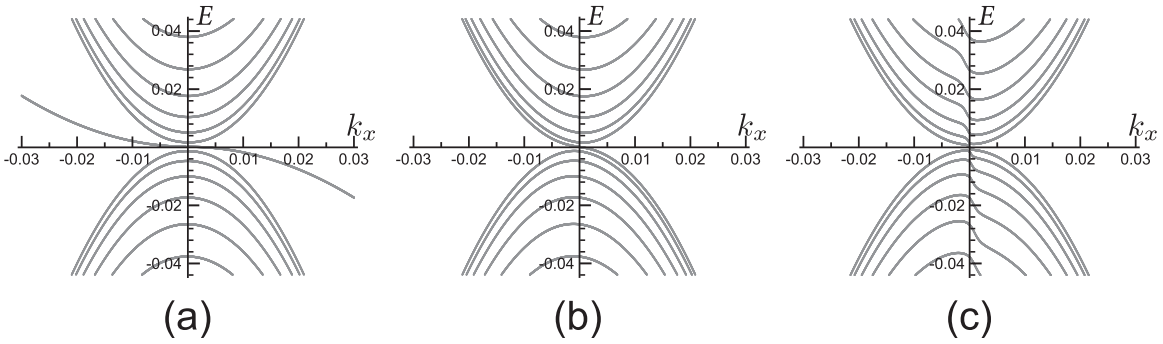

Figure 8. Band structures calculated with a free electron-hole gas Hamiltonian, (2) with $A = M = D = 0$, using band curvature $B = -100$, subject to hard wall boundary conditions at $y = 0$ and the boundary conditions from (31) and (32) at $y = 1000$. The plots differ in the choice of the parameter Q: (a) $Q = -10$, (b) $Q = B = -100$, (c) $Q = -1000$.

and again perform the limits

$$\lim_{M\to-\infty}\left(2B\lambda_1 + A\right)(u_1 + v_1)\sqrt{-M} = 4B\sqrt{-B}\,k_x, \tag{28}$$

$$\lim_{M\to-\infty}\left(2B\lambda_2 + A\right)(u_2 + v_2)\sqrt{-M} = 4B\sqrt{-B}\,k_x, \tag{29}$$

we obtain

$$\begin{aligned}\mathrm{i}\left(v_y\psi^M\right)_2(W) - \mathrm{i}\left(v_y\psi^M\right)_1(W) &= 4Bk_x\left(c_1'\sqrt{-B} + c_2'\sqrt{-B}\right)\\ &= 4Bk_x\psi_1^M(W)\\ &= 2Bk_x\left(\psi_1^M(W) - \psi_2^M(W)\right).\end{aligned} \tag{30}$$

Here, we already made use of the first boundary condition. In total we find, that the boundary to a TI in the limit discussed above can be approximately described by the following boundary conditions, which still contain one free parameter

$$\psi_1(W) = -\psi_2(W), \tag{31}$$

$$\mathrm{i}(v_y\psi)_1(W) - \mathrm{i}(v_y\psi)_2(W) = 2Qk_x\left(\psi_1(W) - \psi_2(W)\right). \tag{32}$$

This parameter was renamed from B to Q, to distinguish it from the band curvature of the material on which we enforce this boundary condition. In this way, we can generalize the case discussed in section 2 and need not restrict ourselves to heterostructures of materials with the same band curvature. Figure 8 shows band structure calculations using the boundary conditions with different choices for the parameter Q. One notes that for $Q = B$ one almost recovers the band structure from figure 2(b) of the main text, which was obtained by a full calculation explicitly including the TI half-plane.

In the derivation, we assumed the TI half plane to extend in the positive y-direction, which is why we matched the exponentially decaying wave functions on the TI side. Of course the same calculation can in principle be redone for an arbitrary interface orientation. E.g., choosing the TI plane to extend in the negative y-direction with a boundary at $y = 0$, leads to the following set of boundary conditions:

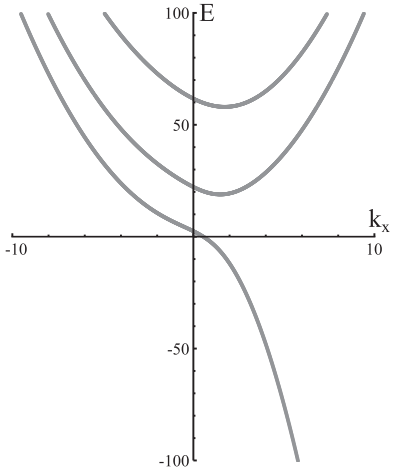

Figure 9. Band structure of a wave guide with a free electron gas Hamiltonian (35) subject to hard wall boundary conditions at $y = 0$, and the Robin boundary condition from (36) at $y = 1$ using $\frac{1}{2}Q = B = 1$.

$$\psi_1(0) = \psi_2(0), \tag{33}$$

$$\mathrm{i}(v_y\psi)_1(0) + \mathrm{i}(v_y\psi)_2(0) = -2Bk_x\left(\psi_1(0) + \psi_2(0)\right), \tag{34}$$

i.e., we find an additional phase factor in front of one wave function component.

This set of boundary conditions also correctly encodes the non-trivial topology in the sense that there will be edge states with a linear dispersion if it is imposed on a topologically trivial insulator, like a gapped electron-hole gas, in which case the group velocity of the emergent edge band will linearly depend on the parameter Q. However, one will not obtain linearly dispersing edge state solutions, if the BHZ-Hamiltonian with a non-trivial topology is subjected to these boundary conditions, which is what one would expect from a heterostructure of two materials which are topologically equivalent.

While (31) and (33) are simple Dirichlet boundary conditions that fix the phase of the two components, (32) and (34) are of the *Robin type* [20], i.e., they link the wave function at the boundary to its derivative. This k_x-dependent mixing induces the PCC in the adjacent metal, as will be shown in the following. To do so, we consider a one-component free electron gas Hamiltonian

$$H = B\left(k_x^2 + k_y^2\right), \tag{35}$$

subject to hard wall boundary conditions at $y = 0$ ($\psi(0) = 0$) and a one-component version of the boundary condition from (32) at $y = W$:

$$\partial_y\psi(W) = -\frac{Q}{B}k_x\psi(W). \tag{36}$$

For $|Q| > |B|$ one obtains a band structures similar to the one shown in figure 9, which has been calculated by setting $\frac{1}{2}Q = B = 1$. It resembles the simple parabolic band structure that one obtains by putting hard wall (or Neumann) boundary conditions on both sides, but it contains an extra band which tends to negative energies with increasing k_x. This creates an unequal number of left and right movers at every Fermi energy, similar to the behavior found for one spin-block

in the case of 2D-TI heterostructures. This imbalance of left and right movers leads to a PCC [21].

While the emergence of large negative eigenvalues is known for Robin problems $\partial_y\psi = -\alpha\psi$ with large negative parameters α [22], as far as we know there has not been a discussion on the emergence of perfecly conducting channels in one-sided Robin wave guides so far.

By implementing this boundary condition, or a similar one (e.g. by replacing k_x in (36) by a different but still odd function of k_x), on one side of a wave guide, one should be able to create PCCs for many scenarios, i.e., for quantum as well as electromagnetic wave guides.

5. Conclusion

To summarize, we demonstrated that the proximity of a 2D TI creates a robust PCC in an adjacent non-topological material. We believe this is a quite general effect that should work for almost all materials with extended states. We expect that a similar phenomenon exists for a disordered conductor at the surface of a 3D TI. We showed that the induction of a PCC can be probed for example in devices based on HgTe/CdTe heterostructures by means of magnetotransport measurements in the ballistic and diffusive regime. In addition, we pointed out that the proximity of a 2D TI to a metal can be understood in terms of a Robin type effective boundary condition, responsible for the creation of the PCC. This does not only allow for simplifications in future theoretical studies, but might also pave the way to induce PCCs by artificially creating such boundary conditions, e.g., by using metamaterials for electromagnetic waves, without relying on TI heterostructures.

Acknowledgments

This work is supported by DFG (SPP 1666 and joined DFG-JST Research Unit FOR 1483 and the funding programme Open Access Publishing). We thank I Adagideli and M Wimmer for useful conversations.

Appendix. Transmission reconstruction

In the manuscript we employed four terminal setups to study the transport properties of PCCs, as sketched in figure A1 . In the following we want to show how the transmission through the metal part T_{M} and the transmission through the TI T_{TI} can be extracted from a set of four terminal resistances. The current I_j through the lead j is generally given by [23]

$$I_j = \frac{e}{h}\sum_k \left(T_{kj}\mu_j - T_{jk}\mu_k \right) \tag{A.1}$$

and depending on the transmissions T_{jk} between lead j and k and the chemical potentials μ_k. The used H-geometry only allows for a vanishing transmission between the leads $1 \leftrightarrow 3$ and $2 \leftrightarrow 4$. This can be employed for an approximate description of the current response

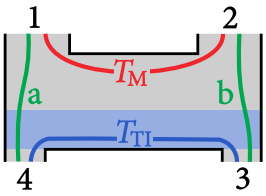

Figure A1. Dominant transport channels of the four terminal setup studied in the manuscript.

$$\vec{I} = \frac{e}{h}\begin{pmatrix} a + T_M & -T_M & 0 & -a \\ -T_M & b + T_M & -b & 0 \\ 0 & -b & b + T_{TI} & -T_{TI} \\ -a & 0 & -T_{TI} & a + T_{TI} \end{pmatrix}\vec{\mu}, \tag{A.2}$$

which is only depending on the two unknown transmissions T_M and T_{TI} and some crosstalk a and b between the opposing leads, as shown in figure A1. This representation of the conductance matrix can only be used at zero or small magnetic fields, as the asymmetry of the off-diagonal elements is neglected. For the small fields considered in our manuscript this is a good approximation. Now we examine the resistances like R_{34}^{12}, which is given by the voltage difference measured between contacts 3 and 4 for a current driven from contact 1 to contact 2. In general there are several possibilities to extract T_M and T_{TI} from a set of four resistance measurements. One possible realization is based on the measurement of

$$R_{34}^{12} = \frac{h}{e^2}\frac{ab}{ab\left(T_{TI} + T_M\right) + (a + b)T_{TI}T_M}, \tag{A.3}$$

$$R_{34}^{23} = \frac{h}{e^2}\frac{aT_M}{ab\left(T_{TI} + T_M\right) + (a + b)T_{TI}T_M}, \tag{A.4}$$

$$R_{41}^{34} = \frac{h}{e^2}\frac{bT_M}{ab\left(T_{TI} + T_M\right) + (a + b)T_{TI}T_M}, \tag{A.5}$$

$$R_{23}^{41} = \frac{h}{e^2}\frac{T_{TI}T_M}{ab\left(T_{TI} + T_M\right) + (a + b)T_{TI}T_M}. \tag{A.6}$$

For this particular set of resistances the transmissions of interest are given by:

$$T_M = \frac{R_{34}^{23}R_{41}^{34}}{R_{34}^{12}\left(\left(R_{34}^{12} + R_{41}^{34}\right)R_{23}^{41} + R_{34}^{23}\left(R_{41}^{34} + R_{23}^{41}\right)\right)}, \tag{A.7}$$

$$T_{TI} = \frac{\left(R_{34}^{12} + 2R_{34}^{23} + R_{41}^{34}\right)R_{23}^{41}}{\left(R_{34}^{12} - R_{41}^{34}\right)\left(\left(R_{34}^{12} + R_{41}^{34}\right)R_{23}^{41} + R_{34}^{23}\left(R_{41}^{34} + R_{23}^{41}\right)\right)}. \tag{A.8}$$

References

[1] Schnyder A, Ryu S, Furusaki A and Ludwig A 2008 *Phys. Rev.* B **78** 195125
[2] Brüne C *et al* 2012 *Nat. Phys.* **8** 485
[3] Bernevig B A, Hughes T L and Zhang S-C 2006 *Science* **314** 1757
[4] König M *et al* 2007 *Science* **318** 766
[5] Ando T and Suzuura H 2002 *J. Phys. Soc. Japan* **71** 2753
[6] Wakabayashi K, Takane Y and Sigrist M 2007 *Phys. Rev. Lett.* **99** 036601
[7] Wurm J, Wimmer M and Richter K 2012 *Phys. Rev.* B **85** 245418
[8] Hutasoit J A and Stanescu T D 2011 *Phys. Rev.* B **84** 085103
[9] Wang X, Bian G, Miller T and Chiang T-C 2013 *Phys. Rev.* B **87** 235113
[10] Yang B-J, Bahramy M S and Nagaosa N 2013 *Nat. Commun.* **4** 1524
[11] Xiao-Guang L *et al* 2013 *Chin. Phys.* B **22** 097306
[12] Rothe D G *et al* 2010 *New J. Phys.* **12** 065012
[13] Bardarson J H 2008 *J. Phys. A: Math. Theor.* **41** 405203
[14] König M *et al* 2008 *J. Phys. Soc. Japan* **77** 031007
[15] Wimmer M and Richter K 2009 *J. Comput. Phys.* **228** 8548
[16] Dorokhov O 1984 *Solid State Commun.* **51** 381
[17] Beenakker C W J 1997 *Rev. Mod. Phys.* **69** 731
[18] Büttiker M 1990 *Phys. Rev. Lett.* **65** 2901
[19] Beenakker C W J and Büttiker M 1992 *Phys. Rev.* B **46** 1889
[20] Gustafson K and Abe T 1998 *Math. Intelligencer* **20** 63
[21] Barnes C, Johnson B L and Kirczenow G 1993 *Phys. Rev. Lett.* **70** 1159
[22] Levitin M and Parnovski L 2008 *Math. Nachr.* **281** 272
[23] Büttiker M 1986 *Phys. Rev. Lett.* **57** 1761